Understanding multi-layered transmission matrices - supplementary file

Anat Levin and Marina Alterman
Department of Electrical and Computer Engineering, Technion
Haifa, Israel

1. Spectra coverage in the weakly scattering case

We start our derivation by considering a weakly scattering volume, expanding the analysis in Sec. 4 of the main paper. Our goal is to understand how the reconstruction error is scaled as a function of the number of fitted layers.

As derived in the main paper under a weakly scattering (first-Born) approximation the Fourier representation of the Transmission matrix corresponds to an entry from the Fourier transform of the RI volume. The wavefront scattering toward direction $\bar{\boldsymbol{\omega}}^v$ when illuminated by an incoming plane wave at direction $\bar{\boldsymbol{\omega}}^i$ is proportional, up to a multiplicative factor, to [5, 6, 8]:

$$\propto \int \boldsymbol{n}(\mathbf{r}) e^{2\pi i (\bar{\boldsymbol{\kappa}}^i - \bar{\boldsymbol{\kappa}}^v)\cdot \mathbf{r}} d\mathbf{r}, \tag{1}$$

with $\bar{\boldsymbol{\kappa}}^v = 1/\lambda \bar{\boldsymbol{\omega}}^v$, $\bar{\boldsymbol{\kappa}}^i = 1/\lambda \bar{\boldsymbol{\omega}}^i$.

As derived in the main paper, since only a subset of frequencies inside a butterfly shape can be measured, for an exact, error-free reconstruction, the minimal Fourier range and primal spacing are

$$\Lambda^* = \mathbf{NA}\boldsymbol{\Omega_f}, \quad \Delta_z{}^* = \frac{1}{\mathbf{NA}\boldsymbol{\Omega_f}} = \frac{\lambda}{\mathbf{NA}^2}. \tag{2}$$

For a scattering volume of thickness d, the number of required layers is:

$$M^* = \frac{d \cdot \mathbf{NA}^2}{\lambda}. \tag{3}$$

In a physical wavefront shaping system we want to approximate the volume with a sparse set of slices, below this optimal bound. Our goal here is to analyze how much error is introduced by such sparse approximations. For that, consider a scattering sample of thickness d, which we try to approximate using $M < M^*$ layers separated by $\Delta_z = \frac{d}{M}$. We denote by $\boldsymbol{\mathcal{E}}_M$ the reconstruction error of a given transmission matrix with the best M layers

$$\boldsymbol{\mathcal{E}}_M = \min_{\boldsymbol{\rho}_1,\ldots,\boldsymbol{\rho}_M} \|\boldsymbol{\mathcal{T}}_{\text{exact}} - \boldsymbol{\mathcal{T}}(\boldsymbol{\rho}_1,\ldots,\boldsymbol{\rho}_M)\|^2. \tag{4}$$

Our goal is to show that $\boldsymbol{\mathcal{E}}_M$ decays relatively fast with M and we can get a reasonable approximation to the transmission matrix even if the number of layers is significantly lower than the exact prediction in Eq. (3). This is a result of two main properties: (i) The volumes describing realistic tissue samples have more energy in the low frequencies; and (ii) the structure of the missing cone implies that, in any case, a significant portion of the spectrum is not sampled by the transmission matrix.

To understand this, consider a naive selection of M layers $\boldsymbol{\rho}_1,\ldots,\boldsymbol{\rho}_M$. Rather than actually solving an optimization problem, we use the ground truth volume $\hat{\boldsymbol{n}}(\boldsymbol{\kappa})$, and simply set to zero any frequency content of the RI volume $\hat{\boldsymbol{n}}(\boldsymbol{\kappa})$ at κ_z values larger than the possible Nyquist range

$$\Lambda^M = \frac{1}{\Delta_z} = \frac{\lambda M}{d}, \tag{5}$$

and we then Fourier transform $\hat{\boldsymbol{n}}(\boldsymbol{\kappa})$ to $\boldsymbol{n}(\mathbf{r})$ and sample planes at spacing $\Delta_z = d/M$. The error of this approximation is basically the integral of content above the cut-off Λ^M. Since according to Eq. (5), the cut-off frequency Λ^M scales linearly with the number of layers, the portion of the spectrum which is lost by this low-pass operation scales linearly with the number of layers M. Thus, the naive answer is that the error of a multi-slice approximation decays linearly with M. In practice we show below that the error decays much faster, since *large areas from the 3D spectrum of the sample are not used by the transmission matrix.*

To gain intuition, consider Fig. 1(b). We note that the butterfly shape is such that low 2D frequencies (i.e. low $|\boldsymbol{\kappa}_{xy}|$), also span less content along the κ_z axes, and hence these frequencies are not lost even with low bandwidths Λ^M. For the higher $|\boldsymbol{\kappa}_{xy}|$ frequencies, the lower κ_z part, marked in dashed blue in Fig. 1(b) is preserved, while the higher portion marked in red is lost.

Another important property of tissue is that its RI is locally smooth, and therefore if we look at its spectrum, we have much more energy in low frequencies than in high ones. Therefore, in the red areas of Fig. 1(b) that are not sampled by the transmission matrix, there is less energy than in the lower frequencies. Thus, despite the fact that the multi-slice approximation sacrifices such frequencies, not much energy is being lost.

In most cases, it is hard to give analytic formulas for the decay of $\boldsymbol{\mathcal{E}}_M$ as a function of M. We can derive an analytic prediction in a simplified model where we assume that the spectrum of $\hat{\boldsymbol{n}}(\boldsymbol{\kappa})$ has random values that are sampled from a uniform distribution for any frequency below a cut-off $\boldsymbol{\Omega_n}$ (i.e. any frequency satisfying $\|\boldsymbol{\kappa}\| \le \boldsymbol{\Omega_n}$), and zero content outside this band. Under this model we can prove

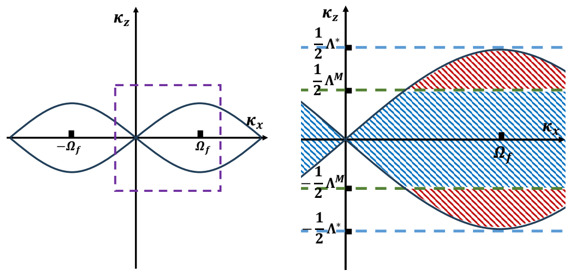

(a) (b)

Figure 1. **Spectrum structure:** (a) An xz slice out of the spectrum of $\hat{\boldsymbol{n}}(\boldsymbol{\omega})$. Entries of a weakly-scattering transmission matrix limited by an aperture **NA** only lie inside the butterfly area. (b) Zooming on the center right area of (a) (purple square). Assuming the ω_z axis is cut at $\pm\frac{1}{2}\Lambda^M$, the transmission matrix entries inside the dashed blue area are maintained, and the entries in the dashed red area are lost.

that $\boldsymbol{\mathcal{E}}_M$ decays at least *quadratically* fast with M. This is a non-trivial result since the cut-off frequency Λ^M scales only *linearly* with M, see Eq. (5). Thus, if we just rely on Nyquist theory and compute the energy of the spectrum above the cut-off frequency, we expect the error to decay linearly with M. The fact that the error decays quadratically with M results from the butterfly structure. However, we emphasize that this result uses the over-simplified assumption of a uniform content in $\hat{\boldsymbol{n}}(\boldsymbol{\kappa})$. In the numerical simulation we see that this result is over-pessimistic, and with more realistic forward scattering volumes, the decay of $\boldsymbol{\mathcal{E}}_M$ is significantly faster than a quadratic function.

Claim 1 *The reconstruction error of a transmission matrix corresponding to a weakly scattering volume with a uniform spectrum, is bounded by*

$$\boldsymbol{\mathcal{E}}_M \leq \left(\frac{M^* - M}{M^*}\right)^2 \boldsymbol{\mathcal{E}}_0, \tag{6}$$

where $\boldsymbol{\mathcal{E}}_0$ is our ability to approximate a transmission matrix with no correction, namely with the ballistic light alone.

We start with a numerical evaluation of this claim and then proceed to the proof.

Numerical validation: To test the decay of the multi-slice fitting error as a function of the number of layers M, we generated synthetic transmission matrices. We used two types of RI volumes, in the first case we selected random values for the spectrum $\hat{\boldsymbol{n}}(\boldsymbol{\kappa})$, for any frequency $\|\boldsymbol{\kappa}\| \leq \boldsymbol{\Omega_n}$, using a band $\boldsymbol{\Omega_n} = 0.3/\lambda$. The second type of RI volume $\boldsymbol{n}(\mathbf{r})$ is filled with a set of spheres at random positions, and each sphere has a random RI different than that of the leading medium. This is a more realistic approximation to the structure of real tissue where we have cells with a certain RI embedded in a surrounding medium with a different RI. In Fig. 2(a) we show a slice through the two spectra $\hat{\boldsymbol{n}}(\boldsymbol{\kappa})$ we receive. With the random spheres the spectrum decays more naturally, and we have much more content at low frequencies than at high ones. This is a more realistic approximation to the spectrum of real tissue since the fact that tissue is forward scattering implies that its spectrum should have more content at lower frequencies.

We synthesized a target $\boldsymbol{\mathcal{T}}_{\text{exact}}$ matrix using a multi-slice model where the planes are sampled very densely. We generated a set of sparse multi-slice approximations with increasing M values in two ways. First, we use gradient descent optimization to minimize the fitting error in Eq. (4). Second, we use a naive filtering of the ground truth volume, where we simply set to zero any frequency content at κ_z values larger than the possible Nyquist range $\Lambda^M = \frac{M}{d}$. We start with a low optical depth, and in Fig. 2(b) we plot the square root of the reconstruction error as a function of M. One can see that with a uniform spectrum, the square root of the error indeed decays linearly with M, suggesting that the actual reconstruction error decays quadratically with M. The curves reach a plateau when M exceeds the Nyquist requirements. This validates the prediction of Claim 1. However, with the more realistic forward scattering volume, the decay of the fitting error is *significantly faster* than the analytic quadratic prediction. For both types of volumes the optimization provides better fits with low M values, but for high M values it runs into local minima, and the fitting error it achieves can be higher than the one achieved by naive filtering.

In our plots, the case $M = 0$ refers to no correction at all, so effectively we assume that the transmission matrix is diagonal. The similarity between a diagonal transmission matrix and the target transmission matrix is a measure of the amount of ballistic light.

1.1. Deriving the multi-slice fitting error

Below we proof Claim 1.

Proof: To prove this result we use a brute-force selection of the layers $\boldsymbol{\rho}_1, \ldots, \boldsymbol{\rho}_M$. We simply set to zero any frequency content of the refractive volume $\hat{\boldsymbol{n}}(\boldsymbol{\kappa})$ at $|\kappa_z|$ values larger than the possible Nyquist range

$$\Lambda^M = \frac{1}{\Delta_z} = \frac{\lambda M}{d}, \tag{7}$$

and we then Fourier transform $\hat{\boldsymbol{n}}(\boldsymbol{\kappa})$ to $\boldsymbol{n}$ and sample planes at spacing Δ_z. In the following paragraphs we offer an upper-bound calculation of the number of transmission matrix entries that lie outside the band Λ^M and are hence lost by the low-pass operation. We show this scales quadratically with M.

To perform this calculation we consider Fig. 3. We note that the butterfly shape is such that low 2D frequencies (i.e. low $|\boldsymbol{\kappa}_{xy}|$) also span less content in the κ_z axes, and hence these frequencies are not lost even with low bandwidths Λ. For the higher $|\boldsymbol{\kappa}_{xy}|$ frequencies, the lower κ_z part marked in blue is preserved, while the higher portion marked in red

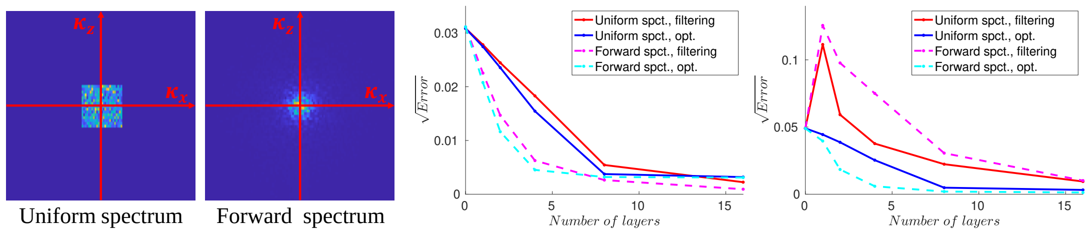

(a) Spectra (b) $OD = 0.5$ (c) $OD = 4$

Figure 2. **Numerical simulation:** We synthesize transmission matrices using a very dense multi-layer model, and test how well we can fit them with a sparser set of layers. We compare two types of volumes, whose spectra are illustrated in (a). The first one has a random spectrum sampled from a uniform distribution, and the second corresponds to a forward scattering spectrum with more content at the low frequencies. We plot the square root of the fitting error as a function of the number of layers. As predicted in claim 1, with a uniform spectrum this decays linearly with the number of layers until we pass the Nyquist limit. The error with the more realistic forward scattering spectrum decays much faster, but analytic characterization is harder. We compute the layers using a naive filtering of the ground truth as well as using gradient descent optimization. The naive filtering provides good results at low optical depths, as illustrated in (b), but fails at higher ODs as illustrated in (c).

in Fig. 3(b) is lost. Below we preform a conservative calculation of how many transmission matrix entries are included in the red area, and show that this number is bounded by a quadratic function of $(M^* - M)$. Using the assumption that the frequency content of the volume is smaller than the cut-off frequency set by the numerical aperture ($\boldsymbol{\Omega_n} < \boldsymbol{\Omega_f}$) we can approximate the butterfly boundaries at areas where the volume has content as linear curves:

$$|\kappa_z| \leq \mathbf{NA}|\boldsymbol{\kappa}_{xy}|. \tag{8}$$

Also, if $\boldsymbol{\Omega_n} < \boldsymbol{\Omega_f}$ the maximal κ_z frequency at which we observe content does not get to $\mathbf{NA}\boldsymbol{\Omega_f}/2$ as derived in Eq. 8 of the main paper, but can be actually reduced to $\mathbf{NA}\boldsymbol{\Omega_n}$. Thus, for error-free reconstruction it is enough to maintain content up to a cut-off frequency of

$$\frac{1}{2}\Lambda^* = \mathbf{NA}\boldsymbol{\Omega_n}, \tag{9}$$

and as a result the minimal number of required layers is

$$M^* = 2\mathbf{NA}\boldsymbol{\Omega_n} d \tag{10}$$

With this model we treat the red area as a triangle, and we denote the frequency at which the triangle intersects with the z-axis bandwidth as κ^M, it can be shown that

$$\kappa^M = \frac{\Lambda^M}{2\lambda\mathbf{NA}} = \frac{M}{2\mathbf{NA}d}. \tag{11}$$

To compute the number of transmission matrix entries in the red region, we need to compute an integral of the following form

$$\int_{\kappa=\kappa^M}^{\boldsymbol{\Omega_n}} \mathbf{NA}(\kappa - \kappa^M) \cdot (2\pi\kappa) \cdot f(\kappa) d\kappa. \tag{12}$$

The first term in this integral is the distance of the triangle from the cutoff frequency (the triangle at frequency $|\boldsymbol{\kappa}_{xy}| = \kappa$ spans κ_z values in a range from $\mathbf{NA}\kappa^M$ to $\mathbf{NA}\kappa$), the 2nd term encodes the fact that in the 3D Fourier domain there is a full circle of frequencies with norm $|\boldsymbol{\kappa}_{xy}| = \kappa$. Finally the function $f(\boldsymbol{\kappa})$ encodes the density of transmission matrix entries which are mapped to frequency $\boldsymbol{\kappa} = (\kappa_x, \kappa_y, \kappa_z)$. Below we show this is bounded by

$$f(\boldsymbol{\kappa}) \leq \frac{c}{|\boldsymbol{\kappa}_{xy}|} \tag{13}$$

where c is a constant scalar. With this we can bound the volume of missing frequencies as

$$\int_{\kappa=\kappa^M}^{\boldsymbol{\Omega_n}} \mathbf{NA}(\kappa - \kappa^M) \cdot (2\pi) \cdot c d\kappa = \mathbf{NA}\pi c \left(\boldsymbol{\Omega_n} - \kappa^M\right)^2 \tag{14}$$

By plugging $\boldsymbol{\Omega_n}$ from Eq. (10), and the value for κ^M as in Eq. (11) we get that the density of transmission matrix entries in the filtered red volume is proportional to

$$\int_{\omega=\omega^M}^{\frac{1}{2}\boldsymbol{\Omega_n}} \mathbf{NA}(\omega - \omega^M) \cdot (2\pi) \cdot c d\omega \propto (M^* - M)^2. \tag{15}$$

Using the same reasoning when we have $M = 0$ layers the error in reconstructing the transmission matrix, namely the full volume of the butterfly shape is proportional $(M^*)^2$. This leads us to the desired Eq. (6).

The last thing we need to prove is that the density of transmission matrix entries around the 3D frequency $\boldsymbol{\kappa} = (\kappa_x, \kappa_y, \kappa_z)$ is bounded by

$$f(\boldsymbol{\kappa}) \leq \frac{c}{|\boldsymbol{\kappa}_{xy}|} \tag{16}$$

For that we recall that we sample a frequency $\boldsymbol{\kappa}$ when we have illumination and viewing directions whose frequencies satisfy $\bar{\boldsymbol{\kappa}}^i - \bar{\boldsymbol{\kappa}}^v = \boldsymbol{\kappa}$, where $\bar{\boldsymbol{\kappa}}^i = 1/\lambda\bar{\boldsymbol{\omega}}^i, \bar{\boldsymbol{\kappa}}^v = 1/\lambda\bar{\boldsymbol{\omega}}^v$, so $\bar{\boldsymbol{\kappa}}^i, \bar{\boldsymbol{\kappa}}^v$ are vectors of norm $1/\lambda$. For that consider illumination and viewing directions which we parameterize using a

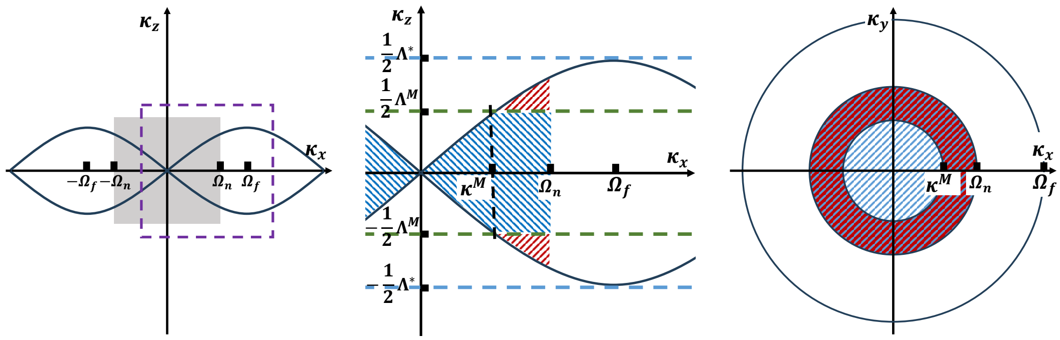

(a) (b) (c)

Figure 3. **Spectrum structure:** (a) an $x - z$ slice out of the spectrum of $\hat{\boldsymbol{n}}(\boldsymbol{\omega})$. Entries of the transmission matrix limited by an aperture **NA** only lie inside the butterfly area. We also assume the content of $\hat{\boldsymbol{n}}(\boldsymbol{\omega})$ is limited to a bend of support $\boldsymbol{\Omega_n}$ marked in gray in the figure. (b) zooming on the center right area of (a) (purple rectangle), assuming the ω_z axis is cut at $\pm\frac{1}{2}\Lambda$, the transmission matrix entries inside the dashed blue area are maintained, and the entries in the dashed red area are lost. The approximation error with M layers is proportional to the red volume, which is shown to scale quadratically with M. (c) The $x - y$ projection of the maintained/lost areas.

2nd order approximation as

$$\bar{\boldsymbol{\kappa}}^i = \begin{pmatrix} \tau_x + \kappa_x \\ \tau_y + \kappa_y \\ \frac{1}{\lambda} - \frac{\lambda}{2}((\tau_x+\kappa_x)^2 + (\tau_y+\kappa_y)^2) \end{pmatrix} \quad (17)$$

$$\boldsymbol{\omega}^v = \begin{pmatrix} \tau_x \\ \tau_y \\ \frac{1}{\lambda} - \frac{\lambda}{2}(\tau_x^2 + \tau_y^2) \end{pmatrix} \quad (18)$$

The difference between these two vectors in the first two coordinates is κ_x, κ_y. The difference in the 3rd coordinate can be expressed as

$$\begin{aligned} \kappa_z &= \lambda(\tau_x\kappa_x + \tau_y\kappa_y) - \frac{\lambda}{2}|\boldsymbol{\kappa}_{xy}|^2 \\ &= \lambda((\tau_x, \tau_y)\cdot(s^1|\boldsymbol{\kappa}_{xy}|)) - \frac{\lambda}{2}|\boldsymbol{\kappa}_{xy}|^2 \end{aligned} \quad (19)$$

where in the right hand side of the above equation we use the 2D unit norm vector $s^1 = (\kappa_x, \kappa_y)/|\boldsymbol{\kappa}_{xy}|$. With this notation we see that to get the 3D frequency κ_z we need to use viewing directions whose τ_x, τ_y satisfy the linear constraint

$$((\tau_x, \tau_y)\cdot s^1) = \frac{1}{|\boldsymbol{\kappa}_{xy}|}\left(\kappa_z + \frac{1}{2}|\boldsymbol{\kappa}_{xy}|^2\right). \quad (20)$$

The density of directions satisfying this constraint scales as $1/|\boldsymbol{\kappa}_{xy}|$.
□

2. Spectra coverage under multiple scattering

The analytical analysis in the main paper has assumed the sample is weekly scattering. While it is hard to give analytical results in the case of multiple scattering, it appears that when the optical depth of the tissue is moderate, light paths undergo a small number of scattering events without being completely scrambled, and the same results hold. The reason is that, since tissue is forward-scattering, light only scatters at small angles. Therefore, after a small number of scattering events, most light paths remain within the butterfly area of the spectrum. This is usually the regime that wavefront-shaping algorithms like [1, 2] attempt to tackle as such algorithms attempt to push the depth at which conventional microscopes can see, but they do not yet attempt to image extremely deep where scattering is fully diffused.

To illustrate this, we carry a Monte-Carlo path tracing through a volume. We consider light paths of the form $\vec{\mathbf{r}} = \mathbf{r}_0, \mathbf{r}_1, \ldots, \mathbf{r}_\ell$, and denote the direction of the ray between points $\mathbf{r}_k, \mathbf{r}_{k-1}$ by $\bar{\boldsymbol{\omega}}_k$. That is, when a light path scatters at a point $\mathbf{r}_k$ it is changing its direction from $\bar{\boldsymbol{\omega}}_k$ to $\bar{\boldsymbol{\omega}}_{k+1}$, see illustration in Fig. 4(a). This is equivalent to sampling the 3D frequency $\boldsymbol{\kappa} = 1/\lambda(\bar{\boldsymbol{\omega}}_{k+1} - \bar{\boldsymbol{\omega}}_k)$. Our Monte-Carlo simulation samples the first direction on the path anywhere inside the numerical aperture of the expected illumination objective. We sample paths according to a target phase function and optical density but discard all paths that eventually exit the volume at directions outside the numerical aperture as such paths cannot be collected by the imaging objective. However, the inner nodes on the path can include scattering at large angles beyond the **NA**. After tracing multiple paths through the volume we compute a histogram of the traced 3D frequencies and we visualize a κ_x, κ_z slice through it. In Fig. 4(b-d) we plot a few such histograms. We start by setting the optical depth of the volume to $OD = 0.5$ (Fig. 4(b)), in this case most paths scatter only once and indeed most of the histogram content is inside the butterfly shape of Fig. 3(a). There is some content outside this ellipse since a few of the paths we traced are longer. In Fig. 4(c) we repeated a similar simulation

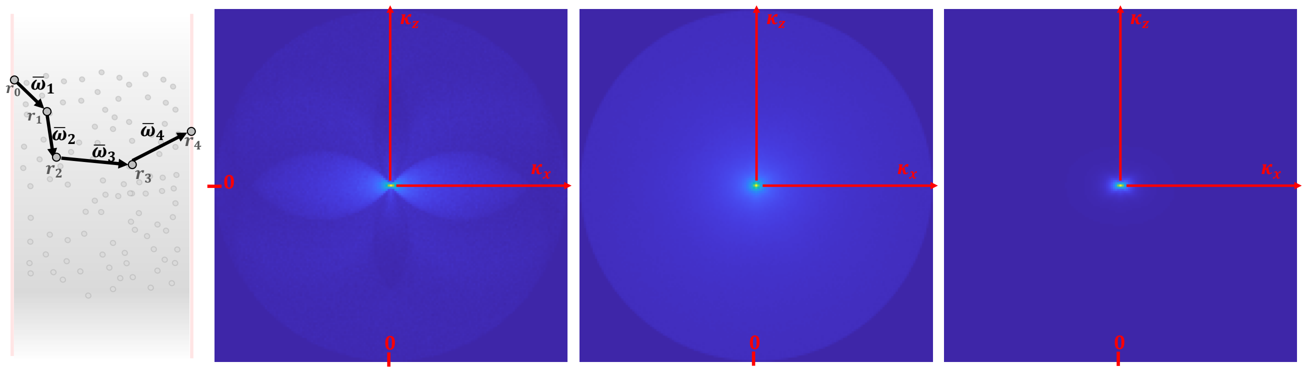

(a) M.C. paths (b) OD=0.5, g=0 (c) OD=5, g=0 (d) OD=5, g=0.9

Figure 4. **3D frequencies of MC paths:** (a) An illustration of a Monte-Carlo path in the volume. (b-d) We plot a histogram of the 3D frequencies traced by such paths. (b) A weakly scattering volume of $OD = 0.5$ with an isotropic phase function, shows most frequencies lie inside a narrow butterfly area. (c) When OD is increased to 5 multiple scattering paths generate content at other frequencies. (d) Even at high optical depths, if the phase function is forward scattering as in tissue, most content is at the low frequencies.

increasing to $OD = 5$, meaning that the average number of scattering events on a path is 5. Such longer paths turn in a variety of directions, and we get content over the entire 3D spectrum. In Fig. 4(b,c) we have assumed that the light is scattering isotropically (Henyey-Greenstein parameter $g = 0$). In Fig. 4(d) we repeated the experiments with $OD = 5$ but used a forward scattering phase function which better describes tissue, with a Henyey-Greenstein parameter $g = 0.9$. Unsurprisingly, most of the paths traced contribute to *low frequencies*, and even though paths are long, most content is inside the butterfly and not in the area of the missing cone. This observation has a significant impact on the analysis of layered approximations: even if they can only capture the low frequencies of the refractive volume, they can still provide a good approximation to the transmission matrix.

2.1. Path tracing with compact support

Due to the large memory requirements of 4D transmission matrices, they are usually only sampled inside a bounded range. That is, we only move illumination point sources inside a small area of size $\mathbf{\Omega_p} \times \mathbf{\Omega_p}$, and measure a bounded set of columns.

When fitting layers, we need to account for the fact that a point/plane illumination scattering through a volume is expanding. Thus, the aberration layers required to explain the transmission matrix are wider than the imaged area of size $\mathbf{\Omega_p} \times \mathbf{\Omega_p}$, see Fig. 5(a). Such compact support transmission matrices can be fitted with a sparser set of layers. To see this we consider Fig. 5(b). Expressing a transmission matrix with a compact support at the frequency basis is equivalent to illuminating the sample with plane waves spanning a wide set of angles, but all the waves pass through a narrow aperture of size $\mathbf{\Omega_p} \times \mathbf{\Omega_p}$. In this case most points inside the volume usually do not receive light from all angles. In Fig. 5(c) we plot the narrow cone of angles arriving at three different points (a ray leaving a point $\mathbf{p_j}$ at direction $\bar{\boldsymbol{\omega}}$ is included in the cone only if this ray is not cropped by the aperture at the back of the sample). Since the cone of light reaching each point is narrower than the full numerical aperture, a local Fourier transform would not have content over the full butterfly area, but cover an even lower range of axial ω_z frequencies. Hence, following the analysis in the previous section, it can be sampled with fewer layers.

To illustrate this, we use again Monte-Carlo path tracing. In Fig. 5(d) we plot the histogram of frequencies visited by a M.C. process, but we only record the paths that passed in three local regions marked in Fig. 5(c). Comparing these histograms to the histogram of paths in the entire volume, we see that the local histograms have a much narrower axial range.

As another way to understand it, we show in Fig. 4 of the main paper an xz slice from the ground truth RI volume and from a few reconstructions. We first optimized for a layer fitting with a dense sampling (high layer number M). Even in this case, the axial resolution of the reconstruction is poor, and *the axial resolution reduces* when the support $\mathbf{\Omega_p}$ is low. This explains why lower supports can be fitted with fewer layers. For each of the two supports we also show a sparse fit, with the minimal M value that provides a good prediction of the transmission matrix.

3. Empirical evaluation of multi-slice approximations

In this section we consider a few transmission matrices and check empirically how well we can approximate them with a multi-slice model. We start with numerically sim-

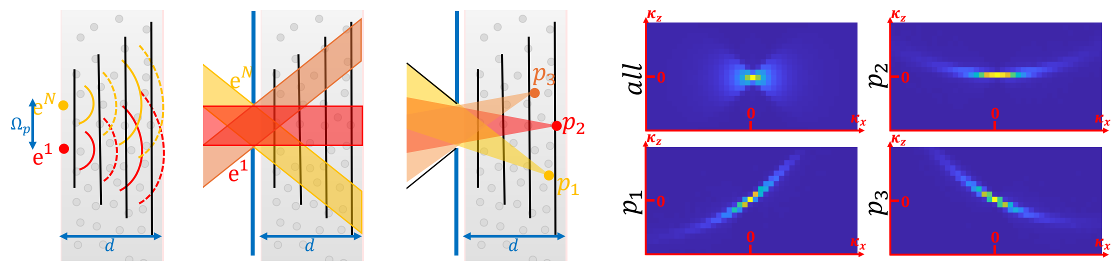

(a) Support primal (b) Support freq. (c) Local directions (d) Path histograms

Figure 5. **Layer support:** (a) as point source expand while propagating through the volume the width of the aberration layers should be wider than the support $\boldsymbol{\Omega_p}$ over which the transmission matrix is measured. (b) To express compact support transmission matrices in the Fourier basis, we illuminate the volume by a set of plane waves passing through an aperture. Such waves also expand through the volume to an area wider then the aperture. (c) The local cone of illumination angles reaching different points inside the volume is much smaller than the actual range of incoming illuminations. (d) Since locally each point receives light through a limited angular cone, the local Fourier transform has a lower axial range. To show this we plot the full histogram of angles scanned by Monte-Carlo paths (this is a zoom of the histograms in Fig. 4). We also plot only the histogram of paths passing through the 3 points marked in (c). One can see that such local path-histograms have a limited axial spread. Due to this limited range they can be explained with fewer layers.

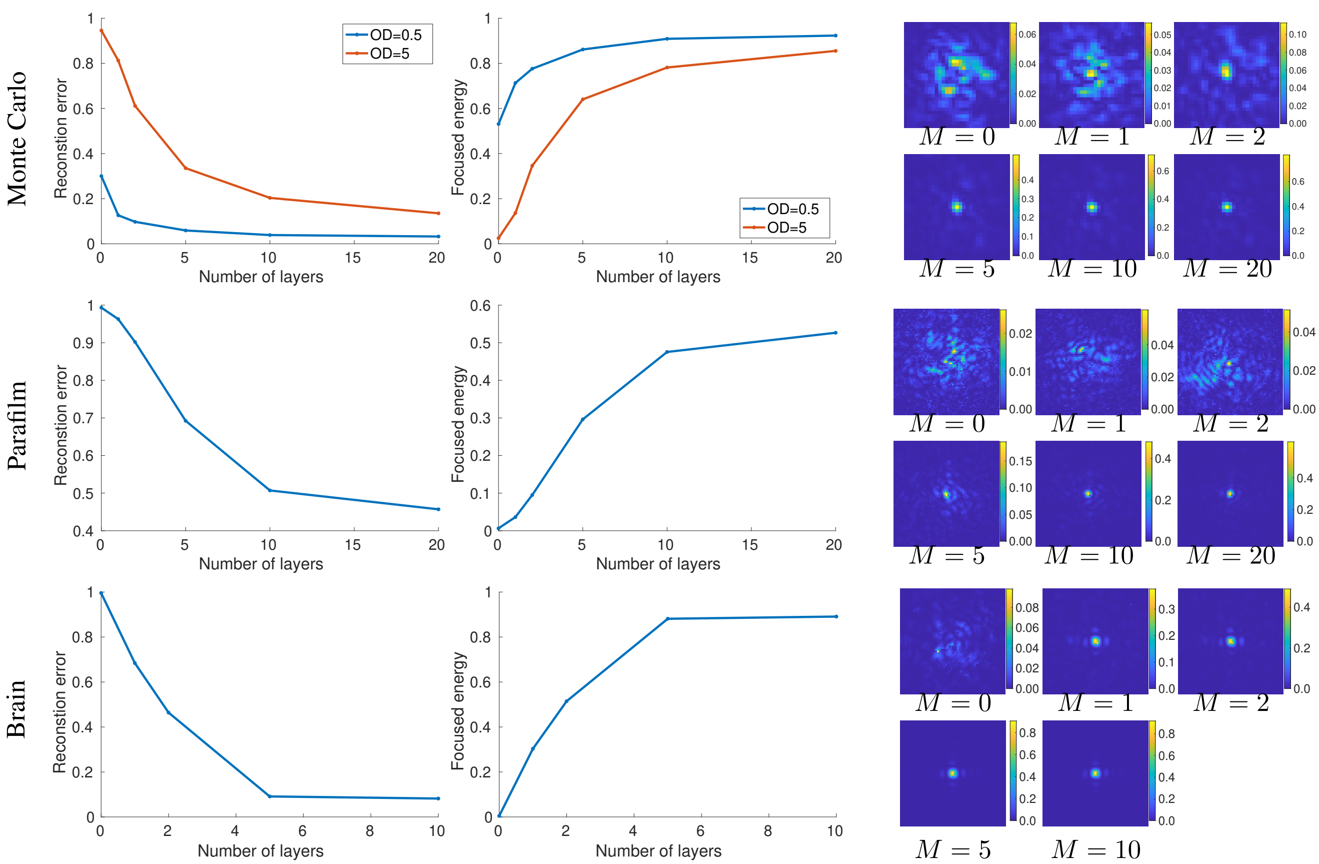

(a) Fitting error (b) Delivered Eng. (c) Focused spots

Figure 6. **Fitting transmission matrix:** We fit a few types of transmission matrices with multi-slice model. The top panel tested physically accurate transmission matrices simulated with the Monte-Carlo approach of [4] at two optical depths. Lower panels used a transmission matrices measured in the lab through layers of parafilm and mouse brain. (a) The reduction in fitting error as a function of the number of layers. (b) The averaged delivered energy (correlation between captured and fitted matrices). (c) An example of a spot behind the tissue using the wavefront estimated by the layered model, with different number of layers. (for the M.C. matrices we only show focusing at $OD = 5$).

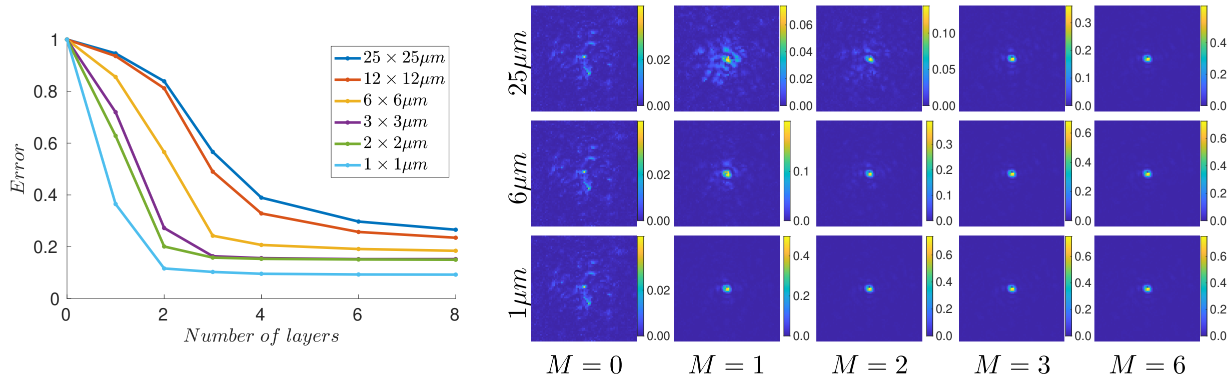

Figure 7. **Layer support for a captured transmission matrix:** We consider a transmission matrix captured in the lab through a chicken breast layer of thickness $170\mu m$. Left: plotting the fitting error as a function of the number of layers. Smaller supports can be fitted with fewer layers. Right: visualization of a spot focusing behind the tissue, computed using the wavefronts of the fitted model. We compare models fitted to different supports. In the top row we need a larger number of layers, but the spot can be scanned over a $25 \times 25\mu m$ window using the same layers. In the lower rows we achieve a focused spot using a smaller number of layers, but these layers can scan the focused spot over smaller windows of sizes $6 \times 6\mu m$ and $1 \times 1\mu m$.

ulated transmission matrices using a more accurate wave-propagation model. We then test lab-captured transmission matrices measuring realistic scattering samples, including thick multiple scattering examples.

While the analysis used the Fourier representation of the transmission matrix, our simulations and measurements use transmission matrices expressed in the primal domain, since in practice, wavefront shaping algorithms use primal measurements.

3.1. Monte-Carlo transmission matrices

The transmission matrices used in the simulations of the previous sections were generated using multi-slice models with very dense slices. The multi-slice model is only an approximation to the full wave-equation because it does not simulate back-scattering paths. To test the discrepancy between this model and the full wave equation, we used the Monte-Carlo algorithm of [3, 4] to synthesize transmission matrices. It has been shown that this algorithm generates complex fields with physically correct statistics which are equivalent to an exact solution to the wave equation, yet it is much faster to compute and scales to much larger scenes. In particular, the M.C. algorithm simulates scattering from particles at any point in the volume (not only on sparse slices) and at all angles (including back-scattering). We simulated a volume of thickness $d = 50\mu m$ at $\lambda = 0.5\mu m$ and illuminated it with point sources spaced over an area of $\boldsymbol{\Omega_p} = 18\mu m$. We measured the scattered fields over a wider support of $30 \times 30\mu m$. We used a forward scattering phase function as is common in real tissue. We simulated volumes with two different optical depths and fitted them with a multi-slice model, while increasing the number of layers. The fit results are plotted in Fig. 6(top). The layered transmission matrices have $\times 7$ lower fitting error when compared to the ballistic term alone which is equivalent to fitting with zero layers. However, even when the number of layers increases and approaches the Nyquist limit, the fitting error does not decrease to zero. This failure is a combination of two issues. First, the fact that the actual transmission matrix includes scattering at wide angles which are not modeled by the layered approximation, and second, the fact that the optimization problem is not convex, and the gradient descent does not converge to a global optimum.

As another way to understand the quality of the fit, we tested the correlation between columns of the exact and fitted transmission matrices and measured

$$\mathcal{C}_M = \frac{1}{K}\sum_k \left| \frac{{\mathbf{t}^k_{\text{exact}}}^T \cdot \mathbf{t}^k_{\text{fit,M}}}{\|\mathbf{t}^k_{\text{exact}}\| \cdot \|\mathbf{t}^k_{\text{fit,M}}\|} \right|^2 \tag{21}$$

where $\mathbf{t}^k_{\text{exact}}, \mathbf{t}^k_{\text{fit,M}}$ are columns from the input and fitted transmission matrices. This provides a prediction of the percentage of energy we can deliver to a point behind the tissue if we use $\mathbf{t}^k_{\text{fit,M}}$ as a wavefront shaping correction, rather than the exact $\mathbf{t}^k_{\text{exact}}$ (note that this only evaluates the energy with respect to the modes included in the input transmission matrix, but there may be additional correction modes not captured by the transmission matrix. Namely, if we would measure a transmission matrix over a wider $\boldsymbol{\Omega_p}$ support we could focus more light to a point). With sufficient M values we can deliver more than 80% of the energy, as plotted in the top row of Fig. 6(b). In Fig. 6(c) we also show some examples of the spot behind the tissue if we use $\mathbf{t}^k_{\text{fit,M}}$ as a wavefront shaping correction. For $M \geq 5$ layers the fit is good enough to provide a sharp spot. Note that while we only show focusing at one point, the layers are optimized such that they allow us to focus at *any point* inside the $\boldsymbol{\Omega_p} \times \boldsymbol{\Omega_p} = 18 \times 18\mu m$ window.

3.2. Acquired transmission matrices

We used the Hadamard algorithm of [7] to capture transmission matrices of real samples in the lab. We measured a layer of parafilm, and two slices of mouse brain and chicken-breast tissue. We measured the parafilm layer to be of thickness $d = 46\mu m$, the mice brain to have thickness $400\mu m$ and the chicken breast to be of thickness $d = 170\mu m$. The transmission matrices cover an area of $\boldsymbol{\Omega_p} = 25\mu m$. The measurement is very noisy, mostly due to vibrations during the long capture. Due to the noisy acquisition the fit is not as good as in the synthetic case, but the fitted wavefronts can still focus more than 50% of the energy and generate sharp spots behind the tissue. We show the fits for the parafilm and brain samples in the two lower panels of Fig. 6. We also show the spot we can get behind the tissue using the approximated transmission matrix. Note that these wavefronts are computed numerically, by multiplying the approximated wavefront by the captured transmission matrix.

In Fig. 7 we show fits on the chicken breast matrix. Here we tested the quality of the fit as a function of ranges $\boldsymbol{\Omega_p}$. For that, the algorithm attempts to fit a subset of the measured columns, limited into smaller spatial ranges $\boldsymbol{\Omega_p}$. As in Fig. 6 of the main paper, we see that smaller spatial ranges can be fitted with fewer layers, since if the transmission matrix only covers a limited spatial support, the range of illumination angles reaching each point in the volume is effectively very narrow, hence locally, the Fourier transform has a limited axial range. From the results in Fig. 7 we can see that for the $25 \times 25\mu m$ support we measured we can obtain good focusing with about $3 - 4$ layers. Fitting a full field-of-view of several hundred microns likely requires additional layers. However, we observe that while using $M = 1$ allows us to focus on a small area of about $2 \times 2\mu m$, with $M = 2$ focus is expanded to a $\times 9$ larger area of $6 \times 6\mu m$, and with $M = 3$, we can focus on an area $\times 150$ larger, reaching $25 \times 25\mu m$. Therefore, using multiple layers can significantly accelerates a sequential scanning of a wide field-of-view.

Mice brain samples used in this manuscript were approved by Institutional Animal Care and Use Committee (IACUC) at the Hebrew University of Jerusalem (MD-20-16065-4).

4. Volume synthesis

To sample the 3D volumes used to simulate multi-layer transmission matrices we sampled spheres at random positions. We sampled the spheres so that the resulting volume would have a target optical depth OD. To this end we had to select two parameters, the sphere density, and the variation in refractive index induced by the sphere.

The sphere radii were uniformly sampled in the range $0.5 - 1.5\mu m$ (so diameters in the range $1 - 3\mu m$) with illumination wavelength $\lambda = 0.5\mu m$. We note that a sphere with radii ς has a 2D cross section area of $\pi\varsigma^2$. Therefore given a target optical depth OD the average number of spheres in a volume of size $W \times W \times d$ should be

$$OD \frac{W^2}{\int p(\varsigma)\pi\varsigma^2 d\varsigma} \tag{22}$$

where $p(\varsigma)$ is the probability of sampling a sphere with radii ς.

Each sampled sphere is assigned a uniform refractive index n, which differs from the refractive index of the leading medium by a random value in the range

$$[-\alpha, \alpha]. \tag{23}$$

We select α so that the resulting volume meets the target optical depth as explained next. To that end we note that the phase masks ρ_m of the multi-slice model in Eq. 2 of the main paper are equivalent to the integral of refractive indices variation in a slice of thickness Δ_z around it. As the refractive index variation has a low magnitude we can approximate the phase mask as

$$\rho_m(x, y) = e^{\frac{2\pi i}{\lambda} n(x,y)} \approx 1 - \left(\frac{2\pi n(x, y)}{\lambda}\right)^2 + i\frac{2\pi n(x, y)}{\lambda} \tag{24}$$

We approximate ρ_m as

$$\rho_m(x, y) = \mu + \delta\rho_m(x, y) \tag{25}$$

such that μ is the mean of ρ (which is a real positive scalar) and $\delta\rho_m(x, y)$ is a zero mean residual. We note that the mean μ is effected by the range of refractive indices α in Eq. (23). On the other hand we note that light propagating through M aberration layers maintains a ballistic component attenuated by μ^M. To meet a target optical depth we want $\mu^M = e^{-OD}$. We therefore numerically scan multiple values of α and select the one providing the desired optical depth.

References

[1] Dror Aizik and Anat Levin. Non-invasive and noise-robust light focusing using confocal wavefront shaping. *Nature communications*, 15(5575), 2024. 4

[2] Dror Aizik, Ioannis Gkioulekas, and Anat Levin. Fluorescent wavefront shaping using incoherent iterative phase conjugation. *Optica*, 9(7):746–754, 2022. 4

[3] Chen Bar, Marina Alterman, Ioannis Gkioulekas, and Anat Levin. A monte carlo framework for rendering speckle statistics in scattering media. *ACM TOG*, 2019. 7

[4] Chen Bar, Ioannis Gkioulekas, and Anat Levin. Rendering near-field speckle statistics in scattering media. *ACM TOG*, 2020. 6, 7

[5] V. Lauer. New approach to optical diffraction tomography yielding a vector equation of diffraction tomography and a novel tomographic microscope. *Journal of Microscopy*, 205 (2):165–176, 2002. 1

[6] Jerome Mertz. *Introduction to optical microscopy*. Cambridge University Press, 2019. 1

[7] S. M. Popoff, G. Lerosey, R. Carminati, M. Fink, A. C. Boccara, and S. Gigan. Measuring the transmission matrix in optics: An approach to the study and control of light propagation in disordered media. *Physical Review Letters*, 104(10): 100601, 2010. 8

[8] Emil Wolf. Three-dimensional structure determination of semi-transparent objects from holographic data. *Optics Communications*, 1(4):153–156, 1969. 1